The E-ELT Design Reference Mission:
The physics and mass assembly of galaxies out to z~6
Results of Simulations

M. Puech, P. Rosati, S. Toft, & A. Cimatti

version	Prepared by	Date	Comments
v0	M. Puech	28/07/08	Very First Draft
v1	M. Puech & P. Rosati	19/09/08	

Contents

1 DRM Science Case: The physics and mass assembly of galaxies out to z∼6

1.1 The science case

[Abstract from P. Rosati et al. proposal:] "We propose to obtain ELT spatially resolved spectroscopy of a sample of a thousand massive galaxies at $2 \leq z \leq 6$, selected from future large area optical-near IR surveys. These observations will yield direct kinematics of stars and gas in the first generation of massive galaxies (in the range $0.1 \leq M_{stellar} \leq 5 \times 10^{11} M_{\odot}$), as well as their stellar population properties. One will be able to derive dynamical masses, ages, metallicities, star-formation rates, dust extinction maps, to investigate the presence of disk and spheroidal components and the importance of dynamical processes (e.g. merging, in/outflows) which govern galaxy evolution. These data will also allow one to study the onset of well known scaling relations at low redshifts, and to witness the gradual shift of star formation from the most massive galaxies in the highest density regions to less massive galaxies in the field. The whole program is designed to provide the ultimate test of galaxy formation theories."

1.2 Goals of the DRM simulations

DRM simulations for the present science case shall focus on the sub-sample of distant emission line galaxies. Due to Signal-to-Noise Ratio (SNR) limitations, absorption line galaxies at $z \gtrsim 1.5$ will more likely be studied using integrated spectroscopy (see Science Case C10-3 "ELT integrated spectroscopy of early-type galaxies at $z > 1$"). Therefore, in the following, only emission line galaxies will be considered and for convenience, we will sometimes use the single word "galaxies" to refer to "emission line galaxies".

Resolved kinematics of such galaxies provides a useful testbed for 3D spectrographs, because it drives the stringent requirements on the SNR: while flux is the zero-order moment of an emission line, the velocity and velocity dispersion are derived from the position and the width of emission lines, which are their first and second moments, and higher order moments always have more relative measurement uncertainty. Hence, DRM simulations shall assess the principal scientific goal of spatially-resolved spectroscopy of distant emission line galaxies, focusing on kinematics. Different objectives can be defined depending on the level of accuracy and/or spatial scale one wants to probe; we have defined the following objectives (dubbed as "steps"), ordered by increasing complexity/difficulty:

1. Simple (3D) detection of emission line galaxies: what stellar mass can we reach at a given SNR as a function of redshift, AO system, environmental conditions, etc.?

2. Recovery of large scale motions (see, e.g., Flores et al. 2006): what are the conditions under which it is possible to recover the dynamical state of distant galaxies (e.g., relaxed rotating disks vs. non-relaxed major mergers)?

3. Recovery of Rotation Curves: what are the conditions under which it is possible to recover the rotation velocity V_{rot} (to derive, dynamical masses or the Tully-Fisher relation, see, e.g., Puech et al. 2006a, 2008) or the whole shape of the RC (for derivation and decomposition in mass profiles, see, e.g., Blais-Ouellette et al. 2001)?

4. Recovery of the detailed kinematics: what are the conditions under which it is possible to detect internal structures in distant galaxies, like clumps in distant disks (see, e.g., Bournaud et al. 2008)?

1.3 Metrics / Figures of merit

As a general metric we will use the total observation time of the survey T_{intg} required to achieve the proposal goals, i.e., observing $\sim$1000 galaxies more massive than $M_{stellar} = 10^{10} M_{\odot}$ in the redshift range 2-6. This high number of galaxies is required to allows us to derive statistics over the morpho-kinematic types of galaxies in several redshift and stellar mass bins (see Sect. 3.3). Given the very ambitious goals of the proposal, they will be considered as met if $T_{intg} \leq 100$ nights. This roughly corresponds to the total time allocated to Large Programs at the VLT per year (30% of the available time). Therefore, such a survey could reasonably be implemented as a several years effort. Finally, this total time should correspond to SNR levels that guarantee to reach at least step 2 for most of galaxies in the survey, and step 4 for a more limited sub-sample (to be defined).

2 DRM Simulations

2.1 Methodology

All input parameters can be separated into two broad categories, namely the "physical" parameter space, which includes all parameters defining the distant galaxy (i.e., redshift z, galaxy diameter, continuum AB magnitude m_{AB}, rest-frame emission line equivalent width EW_0, velocity gradient, morpho-kinematical type), and the "observational" parameter space, which includes the telescope (M1 and M2 sizes, temperature T_{tel}, emissivity ϵ_{tel}), the instrument (spectral resolution R, IFU pixel size Δ_{pix}, detector integration time dit, number of exposures $ndit$, temperatures T_{instr} and emissivities ϵ_{instr}, AO correction, global transmission t_{transm}), and the site (seeing, C_n^2 profile, outer scale of the turbulence L_0, sky brightness and atmospheric transmission).

Given the very large number of parameters to be investigated, as well as the very large range of values to be explored, it is useful to define a "reference case", around which the parameter space can be explored and compared with (see Fig. 1). As such a reference case, we took an M_* galaxy at z=4 observed using MOAO with a seeing of 0.8 arcsec (see Sect. 2.3.1). At this redshift, the [OII] emission line is observed in the H-band, where the influence of the thermal background is minimized in comparison with the K-band. This makes this reference case as independent as possible of the telescope design (e.g., number of mirrors), environmental conditions

(site selection), and instrument characteristics (e.g., number of warm mirrors), which are not all fully known at present.
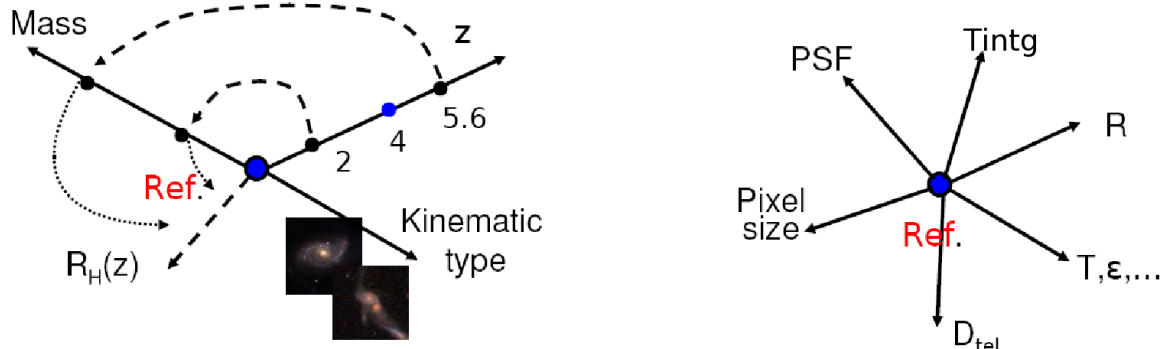

Figure 1: Illustration of the strategy used for exploring the parameter space. A reference case is defined, which is an M_* galaxy at z=4 observed using MOAO with a seeing of 0.8 arcsec (see Sect. 2.3.1). Then, the physical parameter space (on the left), and the observational parameter space (on the right) can be explored relatively to this reference case.

This reference case will be used to assess separately the influence of:

- the AO correction for a given set of other technical and physical parameters;

- the observational parameters for a given set of physical parameters and AO correction;

- the physical parameters for a given set of observational parameters (AO correction included).

2.2 Pipeline

The end-products of 3D spectrographs are data-cubes in FITS format. Hence, we have developed a simulation pipeline that produces such mock data. These fake data are produced assuming a perfect data reduction process, whose impact has therefore been neglected.

2.2.1 General description

Data-cubes are simulated using a backward approach of the usual analysis of 3D data. During such a process, each spaxel is analyzed separately in order to extract from each spectrum the continuum and the first moments of emission lines. One ends up with a set of maps describing the spatial distribution of the continuum and line emissions (zeroth order moment of the emission line), as well as the gas velocity field (first order moment) and velocity dispersion map (second order moment). Such maps are routinely derived from Fabry-Perot observations of local galaxies (see, e.g, Epinat et al. 2008), or can be produced as by-products of hydrodynamical simulations of local galaxies (e.g., Cox et al. 2006). Using simple rules and empirical relations,

5

these maps can be rescaled (in terms of size and total flux) to provide a realistic description of distant galaxies (see Sect. 2.3.1). Assuming a Gaussian shape for all spectra, it is then straightforward to reconstruct a data-cube from such a set of four maps, by "reversing" the usual analysis of 3D data. This allows us to produce a data-cube at high spatial resolution, which can then be degraded at the spatial resolution (AO PSF) and sampling (IFU pixel scale) required for simulating data produced by a given 3D spectrograph. A more detailed description of the process is given below.

2.2.2 High resolution data-cube

At very high spatial resolution, emission lines with kinematics driven only by gravitational motions are well described by simple Gaussians (Beauvais & Bothun, 1999). Under this assumption, within each pixel of the data-cube, only four parameters are needed to fully define a spectral line. The first three parameters are the position in wavelength, the width, and the area (or, equivalently the height) of the emission line. The current version of the software only models emission lines and does not take into account the detailed shape of the continuum in galaxies - it is simply modeled as a constant in f_λ. So only one parameter is required to set the level of this pseudo-continuum around the emission line. Each spectrum is generated in the observational frame, at a given spectral sampling of $\lambda_{obs}/2R$, where R is the spectroscopic power of resolution of the instrument, and $\lambda_{obs} = (1 + z)\lambda_{em}$, λ_{em} being the rest-frame wavelength of the emission line, and z the redshift of the simulated object. During this process, the rest-frame line width is multiplied by $(1+z)$, as one needs to take into account the widening of emission lines with increasing redshift.

All these four parameters can be extracted from observations of local galaxies. In the following, we use Fabry-Perot (FP) observations of the Hα emission distributions of nearby galaxies obtained as part of the GHASP survey (Amram et al., 2002). From these data, we can extract four parameters, wavelength, width, area, and continuum level to construct the velocity field, the velocity dispersion map, the flux map of the Hα emitting gas, and the continuum map of the galaxy. The software first re-scales all these maps at a given angular size (in arcsec) provided by the user. These maps are then interpolated at a spatial sampling of $\lambda_{obs}/2D$. This spatial sampling is motivated by the fact that the AO PSFs used have been simulated at this sampling rate (see below). The software then re-scales the overall amplitude of the continuum map at a given integrated number of photons using an integrated magnitude m_{AB} directly provided by the user. This magnitude is converted to the number of photons per spectral pixel depending on the telescope diameter D, the total integration time T_{intg}, and the global transmission t_{trans} of the system (atmosphere excluded). The overall amplitude of the Hα map is also rescaled at a given integrated number of photons, derived from the integrated continuum value and a rest-frame equivalent width EW_0 provided by the user, the latter being re-scaled in the observed-frame by multiplying by $(1 + z)$. All parameters can also be extracted from outputs of hydro-dynamical simulations (Cox et al., 2006). In this case, the two last parameters (area and continuum level) can respectively be extracted from total gas and stellar surface density maps.

2.2.3 Modeling the IFU and the detector

Each monochromatic slice of the high resolution data-cube is convolved by a PSF with matching spatial sampling. This PSF must be representative of all elements along the optical path, from the atmosphere to the output of an (optional) Adaptive Optic system. Because the isoplanetic patch (Fried 1981; the median value at Paranal is ~2.4 arcsec at $\lambda \sim 0.5\ \mu$m, which leads, e.g., to ~10 arcsec at $\lambda \sim 1.6\ \mu$m) is larger than the individual FoV of the IFU (typically a few arcsec, depending on the size of objects at a given redshift), the same PSF can be used to convolve the data-cube regardless of position within the IFU. We also neglected the variation of the PSF with the wavelength (with a FWHM varying as $\lambda^{-1/5}$ in a Kolmogorov model of the atmospheric turbulence, see, e.g., Roddier 1981), as we are only interested in the narrow spectral range around a single emission line.

The next step is to reduce the spatial sampling of the data-cube. This is done by re-binning each monochromatic channel of the data-cube at the pixel size Δ_{pix} of the simulated IFU. A wavelength dependent atmospheric absorption curve is then applied to each spectrum of the data-cube. Sky continuum, detector dark level, bias, and thermal background are then added to the spectra. Thermal backgrounds are modeled using gray bodies parametrized by a temperature T and an emissivity ϵ, i.e., a black body of temperature T multiplied by a constant emissivity ϵ. Photon and detector noise are then added. In the NIR, the detector noise is due to the dark current ($dark$), and readout noise (RON).

Finally, the simulation pipeline generates $ndit$ data-cubes with individual exposure time of dit, which are combined by estimating the median of each pixel to simulate several individual realistic exposures. Since we have only included random noise, it is similar to having dithered all of individual exposures and combining them after aligning them spatially and spectrally. Sky frames are evaluated separately (i.e., with a different noise realization), and then subtracted to each individual science frame, reproducing the usual procedure in both optical and NIR spectroscopy.

2.2.4 Post-treatment of simulated data-cubes

The simulated data-cubes are analyzed using an automatic data analysis pipeline similar to those generally used to analyze data of high redshift galaxies. During this process, each spatial pixel of the simulated data-cube is fitted with a Gaussian in wavelength, whose position and width correspond respectively to the velocity and velocity dispersion of the gas in this spatial pixel. Because the accuracy on these measurements is driven by the flux within the emission line relative to the noise on the continuum, one has to define a kinematic signal-to-noise ratio SNR_{kin} specific to this measurement. We chose to rely on the definition of Flores et al. (2006), who defined SNR_{kin} as the total flux in the emission line divided by the noise on the continuum $\sigma_{continuum}$ and $\sqrt{N_{pix}}$, the number of pixels within the emission line. We emphasize that this SNR_{kin} is different from the classical SNR: the latter quantifies the signal-to-noise ratio relative to sky and detector noise (detectability of the emission line), while the former characterizes the capability of measuring the first and second order moments of the emission line, relative to the noise in the continuum (Sarzi et al., 2006). Although they are different in nature, we find

that both SNRs roughly correlates provided that $SNR > 3$ (corresponding the $SNR_{kin} \sim$3-4). Tests show that pixels with $SNR_{kin} < 3$ have very large errors mostly due to misidentification of emission lines with noise peaks. Hence, only pixels having $SNR_{kin} \geq 3$ have been considered for further analysis.

2.2.5 Validation experiment

We conducted a special run to compare the simulation pipeline with real 3D observations on the VLT of a galaxy at z~2.4 observed by R. Genzel's group using SINFONI (Genzel et al., 2006). The goal of this run is to use input parameters corresponding to a real observed case and assess whether or not the simulation pipeline is able to produce a data-cube with the same quality, quantified using the median SNR_{kin} (see definition in the previous section). For the z~2.4 galaxy observed with SINFONI, the corresponding input parameters are: size of 0.8 arcsec, K=21.47, $EW_0(H\alpha)$=140Å, T_{intg}=6 hr, pixels of 50×100 mas^2, PSF with FWHM=150 mas, temperature of the telescope and instrument of 287K (VLT), emissivity of the telescope of 6% (Cassegrain focus), emissivity of SINFONI of 15%. We took care of mimicking the SINFONI data reduction procedure by interpolating pixels from the physical 50×100 mas^2 spatial scale to the 50×50 mas^2 final scale, and smoothing down the data-cube to a resolution of 190 arcsec. The results of this validation run are shown in Fig. 2 and demonstrate that, given a complete set of technical and physical parameters, simulations can produce data-cubes with a quality similar to that of real observations. Moreover, the similarity between the observed velocity field and velocity dispersion map (see first line in Fig. 2) and those produced by the automatic analysis pipeline (see second line) shows that the automatic analysis pipeline can be used safely.

2.3 Inputs

All magnitudes are given in the AB system.

2.3.1 Scientific data

Scientific data are needed in order to (1) provide the simulation pipeline with morpho-kinematical templates to be used as inputs and (2) rescale these templates in terms of realistic size, flux, and velocity gradient compared to distant galaxies. A global flowchart of the rescaling procedure is shown in Fig. 3, while specific details are given below.

Morpho-kinematical templates: Table 1 summarizes the main properties of the high resolution templates used for the simulations (see also Fig. 4 and 5).

Redshift: Given the objective of the survey, three redshift "bins" have been considered for simulations. Table 2 summarizes these redshifts with the "observed" emission line. For simplicity, the [OII] emission line was assumed to be a single line centered at 3727Å; this allows us to avoid introducing an additional parameter, i.e.,
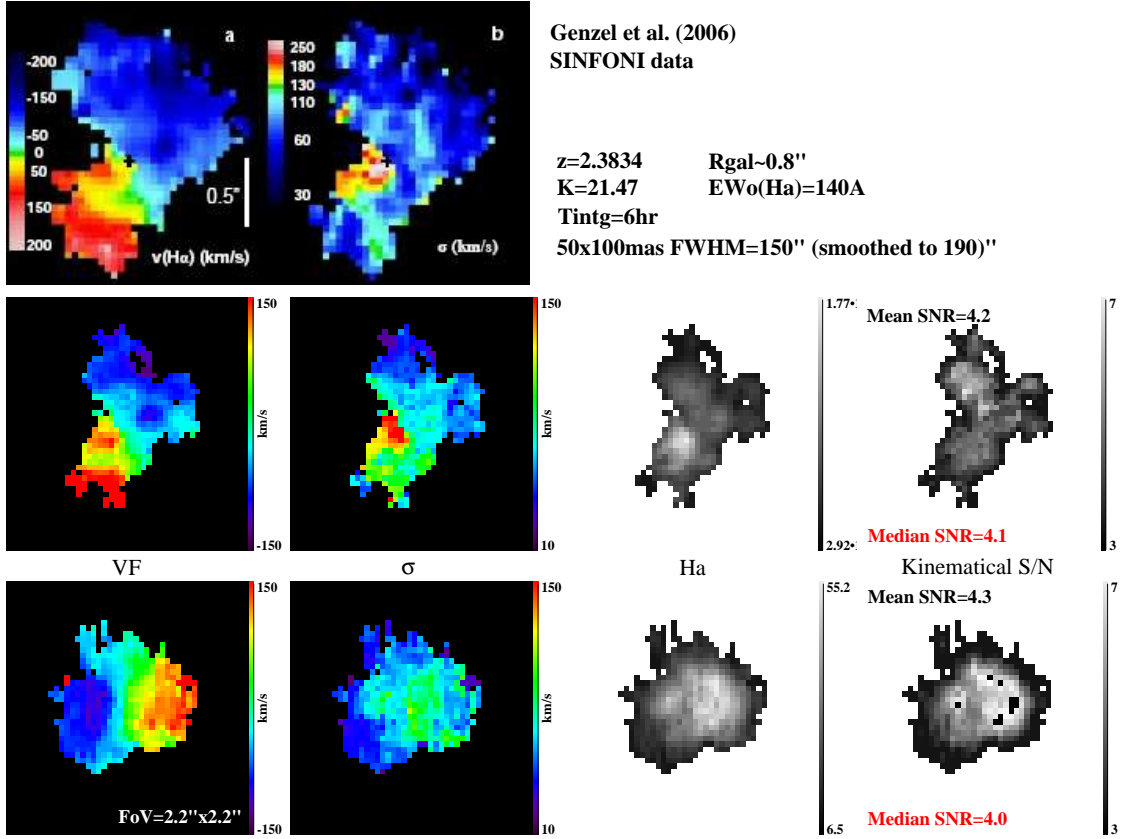
Figure 2: Comparison of SINFONI data with simulations of a rotating disk (UGC5253 template, see Sect. 2.3.1) using the same set of observational and physical parameters (see text). *First line:* SINFONI observations of a z∼2.4 galaxy (*left:* velocity field; *right:* velocity dispersion map). *Second line:* analysis of the reduced SINFONI data-cube (courtesy of N. Förster-Schreiber). *From left to right:* velocity field, velocity dispersion map, Hα map, and SNR_{kin} map. *Third line:* simulations of a rotating disk using the technical and physical parameters corresponding to the real SINFONI observations. The median SNR_{kin} is found to be very similar in both cases.

the line ratio between the lines of the doublet, which depends mostly on the electron density in the medium (Puech et al., 2006a). This does not influence the integrated SNR over the emission line but leads to overestimate the maximal spectroscopic SNR in the emission line. The impact of this assumption will be investigated in Sect. 3.5. Note that the highest redshift considered (z=5.6) corresponds to the limit where [OII] falls within the K-band.

Stellar mass and flux: We used the MUSIC compilation of public spectro-photometric data in the GOODS field (Grazian et al., 2006) to derive empirical relations between redshift, observed K-band magnitude, and stellar-mass $M_{stellar}$ (see Fig. 7). The latter quantity was expressed as a fraction of the characteristic stellar-mass $M_*(z)$ at a given redshift, which describes the knee of the Galaxy Stellar Mass Function (GSMF) at this redshift, according to a Schechter function (see inset
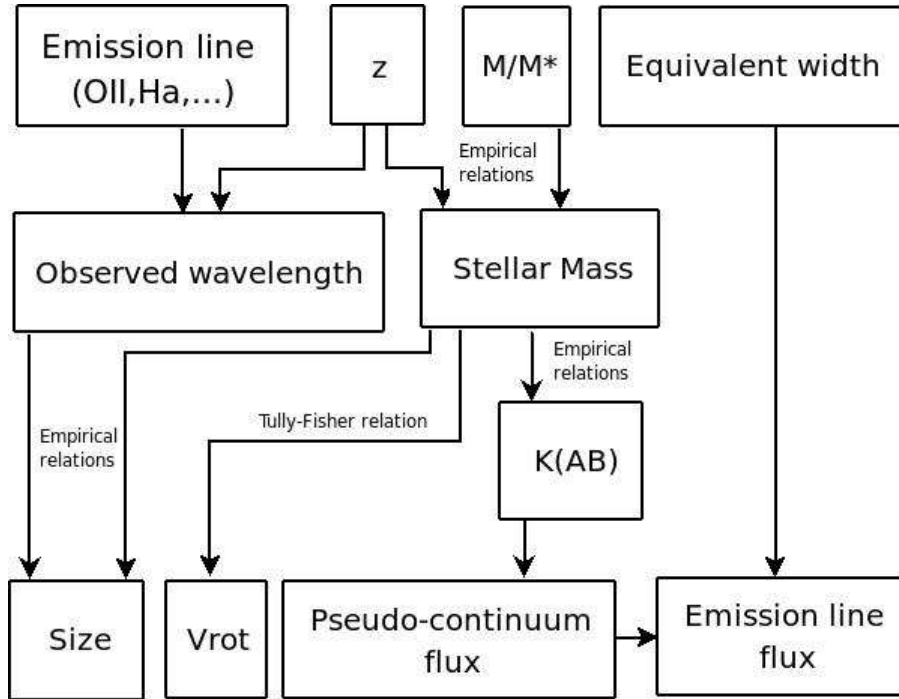
Figure 3: Schematic illustration of the method used to rescale the morpho-kinematical templates in order to make them match the size and flux of distant galaxies. Also, the velocity dispersion (not shown here) can be rescaled using a multiplicative value.

Name	Morphological type	inc (deg)	M_B or $M_{stellar}$	z	Comments
UGC5253	Sab	40	-20.8	0.00441	Rotating disk
UGC6778	SABc	30	-20.6	0.003226	Rotating disk
UGC7278	Im	44	-17.1	0.00097	No rotation
UGC7592	IBm	64	-17.8	0.00069	No rotation
ARP271	SAc-SBc	59/32	-20.6/-21.2	0.0087	Merging pair
Major merger	Sbc-Sbc	69	$5\times10^{10}M_\odot$	0.0	Simulation
Clumpy Disks	—	50	$3\times10^{10}M_\odot$	1.0	Simulations

Table 1: Main properties of the morpho-kinematical templates used for the simulations. The first five templates are real observations from Garrido et al. (2002, 2004) and Fuentes-Carrera et al. (2004), while the two last are hydrodynamical simulations from Cox et al. (2006) and Bournaud et al. (2007). *From left to right:* Name, morphological type, morphological inclination, absolute B-band magnitude or stellar mass for simulations, redshift, and comments.

in Fig. 7). In other words, at a given z, galaxies with stellar mass $M_{stellar} = M_*(z)$ are those that contribute the most to the stellar mass density at this redshift. Table 3 gives the corresponding stellar masses in the simulations as a function of redshift. The pseudo-continuum flux around the emission line is directly derived from the K-band magnitude; we did not apply any "color" correction between the rest-frame wavelength of the emission line (e.g., 0.3727 μm for [OII]) and that of the K-band
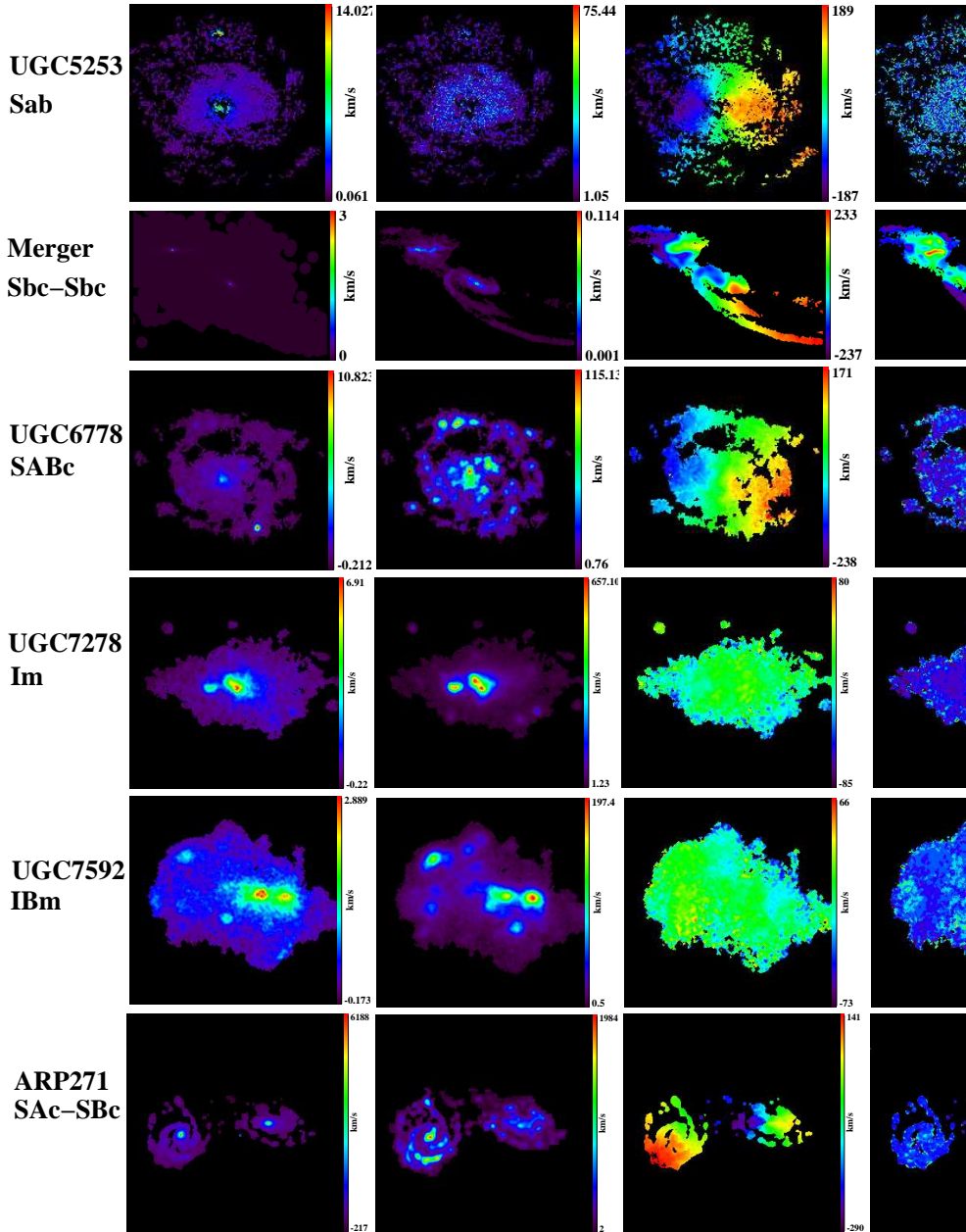
Figure 4: Morpho-kinematical templates used for the simulations. *From left to right:* continuum map, emission line map, gas velocity field, and gas velocity dispersion map. For the major merger simulation, the first two maps are the stellar surface density and the gas surface density maps.

(e.g., 0.44 μm at z=4, see Fig. 6). Such an assumption is consistent with Spectral Energy Distributions of galaxies with a morphological type latter than Sa within a factor two in flux. As a reference case, we adopted a z=4, M_* galaxy (see Sect. 2.1).

Rest-frame emission line equivalent width: We assumed $EW_0([OII])=30$Å, which is an extrapolation of the mean value found at z=1 (Hammer et al., 1997). This parameter does not influence the flux distribution of the galaxy but is used to
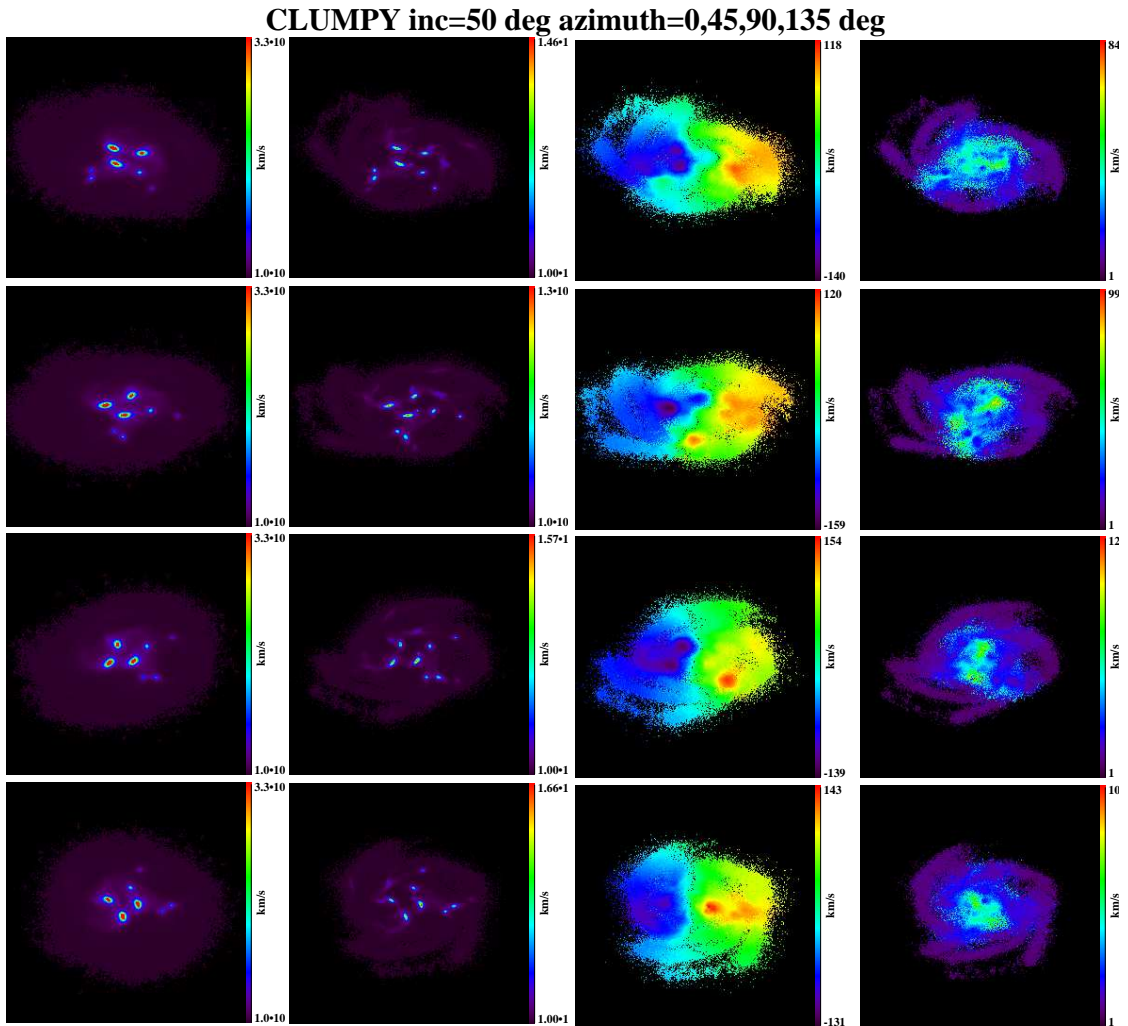
CLUMPY inc=50 deg azimuth=0,45,90,135 deg

Figure 5: Morpho-kinematical templates from simulations of clumpy disks viewed from different azimuthal angles. *From left to right:* stellar surface density map, gas surface density map, gas velocity field, and gas velocity dispersion map.

z	Look-back time (Gyr)	Emission line	Observed broad-band
2.0	10	Hα $\lambda6563$Å	K
4.0	12	[OII]$\lambda3727$Å	H
5.6	12.6	[OII]$\lambda3727$Å	H

Table 2: Redshifts (and look-back-time) considered for simulations, with the corresponding emission line targeted. The last column gives the broad-band filter within which the redshifted emission line falls.

set its total integrated value (see Sect. 2.1).

Size: We used empirical relations between redshift and half-light radius from the literature (see Fig. 8). To mitigate the impact of the different sample selection criteria used at high redshift, we average the different values found in the literature (Bouwens et al., 2004; Ferguson et al., 2004; Dahlen et al., 2007). The resulting
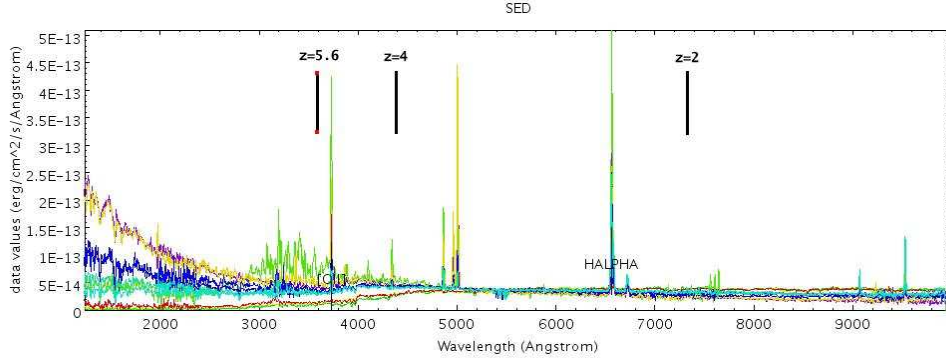
Figure 6: Averaged Spectral Energy Distribution for different morphological classes of local galaxies. *From top to bottom (in the UV):* starbursts with $E(B - V) \leq 0.1$, starbursts with $0.11 \leq E(B - V) \leq 0.21$, starbursts with $0.25 \leq E(B - V) \leq 0.35$, starbursts with $0.39 \leq E(B - V) \leq 0.50$, starbursts with $0.51 \leq E(B - V) \leq 0.60$, Sc galaxies, starbursts with $0.60 \leq E(B - V) \leq 0.40$, Sb galaxies, Sa galaxies, and S0 galaxies (Kinney et al., 1996). The [OII] and Hα emission lines are labeled in the bottom of the spectra. The rest-frame position corresponding to the central wavelength of the K-band (2.2 μm) is indicated at the top, for different redshifts. The difference between the pseudo-continuum around the two emission lines and that corresponding to the rest-frame K-band is smaller than a factor two in flux for types latter than Sa.
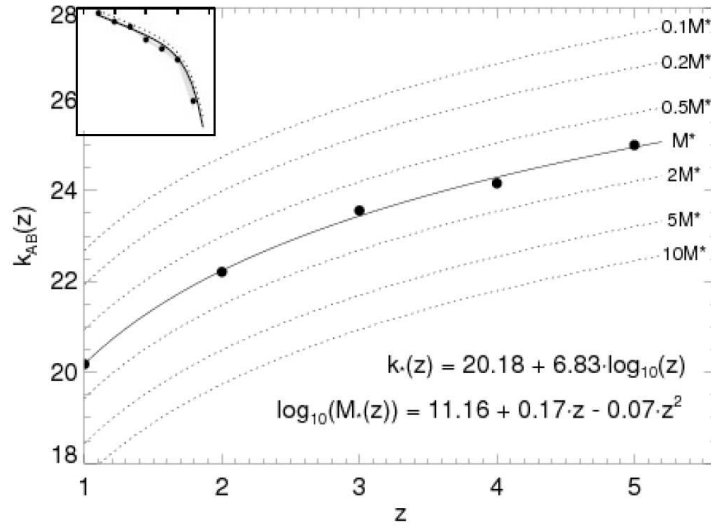
Figure 7: Empirical relations between the observed K-band magnitude and redshift used to rescale the morpho-kinematical templates to make them match the continuum flux of distant galaxies at the corresponding stellar-mass. *Inset:* Illustration of the fit of a Galaxy Stellar Mass Function by a Schechter function. The knee of the curve is called M_*; its variation with redshift is given by the formula on the bottom. The upper formula gives the evolution of the K-band magnitude of an M_* galaxy as a function of redshift.

z	Quantity	$0.1M_*$	$0.5M_*$	$1.0M_*$	$5.0M_*$	$10.0M_*$
2.0	$log(M_{stellar}/M_\odot)$	10.2	10.9	11.2	11.9	12.2
	K_{AB}	24.7	23.0	22.2	20.5	19.7
	ΔV (km/s)	160	210	260	350	430
	Size (arcsec)	0.68	1.19	1.52	2.67	3.40
4.0	$log(M_{stellar}/M_\odot)$	9.7	10.4	10.7	11.4	11.7
	K_{AB}	26.8	25.1	24.3	22.6	21.8
	ΔV (km/s)	130	180	200	300	330
	Size (arcsec)	0.33	0.59	0.75	1.3	1.7
5.6	$log(M_{stellar}/M_\odot)$	8.9	9.6	9.9	10.6	10.9
	K_{AB}	27.8	26.0	25.3	23.5	22.8
	ΔV (km/s)	90	110	140	200	240
	Size (arcsec)	0.28	0.50	0.63	1.11	1.41

Table 3: Stellar mass, K-band magnitude, velocity gradient, and size of the simulated galaxies as a function of redshift.

"mean" half-light radius was then k-corrected using the empirical relation of Barden et al. (2005) (see Fig. 8), and re-scaled to the assumed stellar-mass using the local scaling between the K-band luminosity (used as a proxy for stellar mass) and size reported by Courteau et al. (2007), i.e., $R_{half} \propto L_K^{0.35}$. The total size (diameter) was assumed to be four times the half-light radius. Note that in the case of a exponential thin disk, $R_{25} = 3.2R_d$ and $R_{half} = 1.68R_d$, which approximately leads to $R_{25} \sim 2R_{half}$. The diameters (in arcsec) used in the simulations are given in Tab. 3.
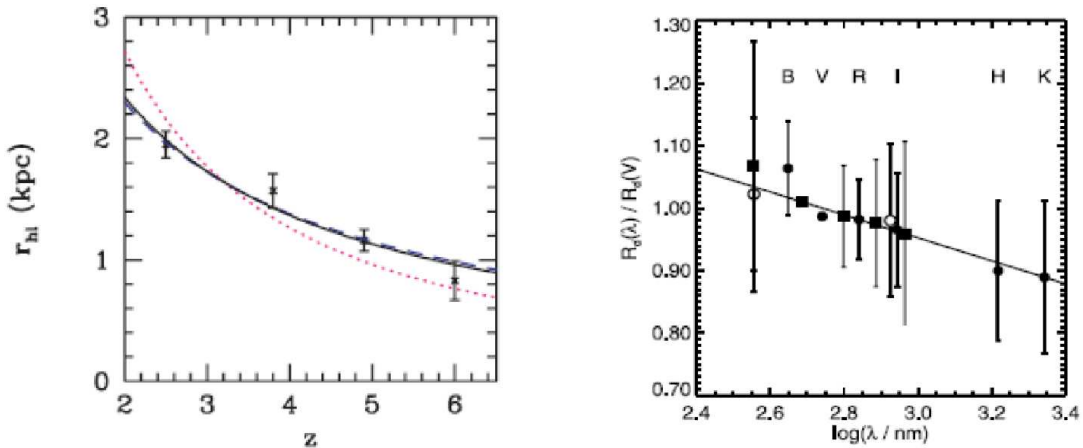
Figure 8: Empirical relations used to rescale the morpho-kinematical templates to make them match the size of distant galaxies at the correct observed wavelength. *Left:* relation between size and redshift from Bouwens et al. (2004). *Right:* relation between size and wavelength from Barden et al. (2005).

Velocity gradient amplitude: The velocity amplitude of the velocity field was rescaled using the local stellar-mass Tully-Fisher Relation, following Hammer et al.

([2007](#)) (see Tab. [3](#)). Note that strictly speaking, this procedure is quantitatively correct only if applied to rotating disk morpho-kinematical templates.

2.3.2   Technical data

All simulations were performed before the official baseline of the E-ELT DRM was defined. Therefore, there are a few differences between the version v1 of the official baseline (see DRM web pages) and the technical inputs actually used in the simulations. The main differences are listed below.

Site and sky background: A Paranal-like site is assumed with T_{site}=280K. Atmospheric absorption is modeled following a Paranal-like site, although at a lower spectral resolution than the official current model. Sky emission (continuum and OH lines) was accounted for using a model from Mauna Kea, which also includes zodiacal emission, thermal emission from the atmosphere, and an average amount of moonlight. Compared to the official DRM models, this Mauna Kea model is two times fainter in the H band than a Paranal-like site. In the K-band, the Mauna Kea sky background model falls in between the official DRM Paranal-like model and the high and dry model. The influence of the sky background will be discussed in Sect. 3.4.2. See the DRM web pages for more details.

Telescope model: We followed the official 42 meter E-ELT 5-mirror design. Its thermal background was modeled using a gray body, and assuming an emissivity of 5% (Ag+Al coating). We neglected the central apperture, as it is not included in the modeling of the PSFs (see below). The collecting area of the telescope is therefore 8% larger that the official baseline.

Instrument model: We assumed a reference pixel size of 50 mas, and a reference spectral power of resolution of R=5000, as a compromise between our desire to minimize the impact of the OH sky lines and not wanting to over-resolve the line by a large factor. The instrument thermal background was modeled using two gray bodies. The first one models the effect of the Target Acquisition System, and assumes a temperature of 240K and an emissivity of 15%. The second one models the effect of the spectrograph, and assumes a temperature of 150K and an emissivity of 69%. These numbers were derived following a preliminary study of the thermal background of EAGLE (Laporte et al., 2008). The instrument background represents less than 10% of the telescope background in both the H and K bands (see Fig. [9](#)), in agreement with the official requirements for EAGLE, which specify that "the instrument thermal background at the detector shall be less than 50% of that from the telescope" (goal=10%). The total background is dominated by the thermal contribution of the telescope in the K band, and by the sky background in the H band. Therefore, we did not explore variations in the thermal contributions from the instrument, which is never the dominant source of background.

Detector model and exposure time: We rely on the description of a cooled Rockwell HAWAII-2RG IR array working at ∼80K, as described by Finger et al.
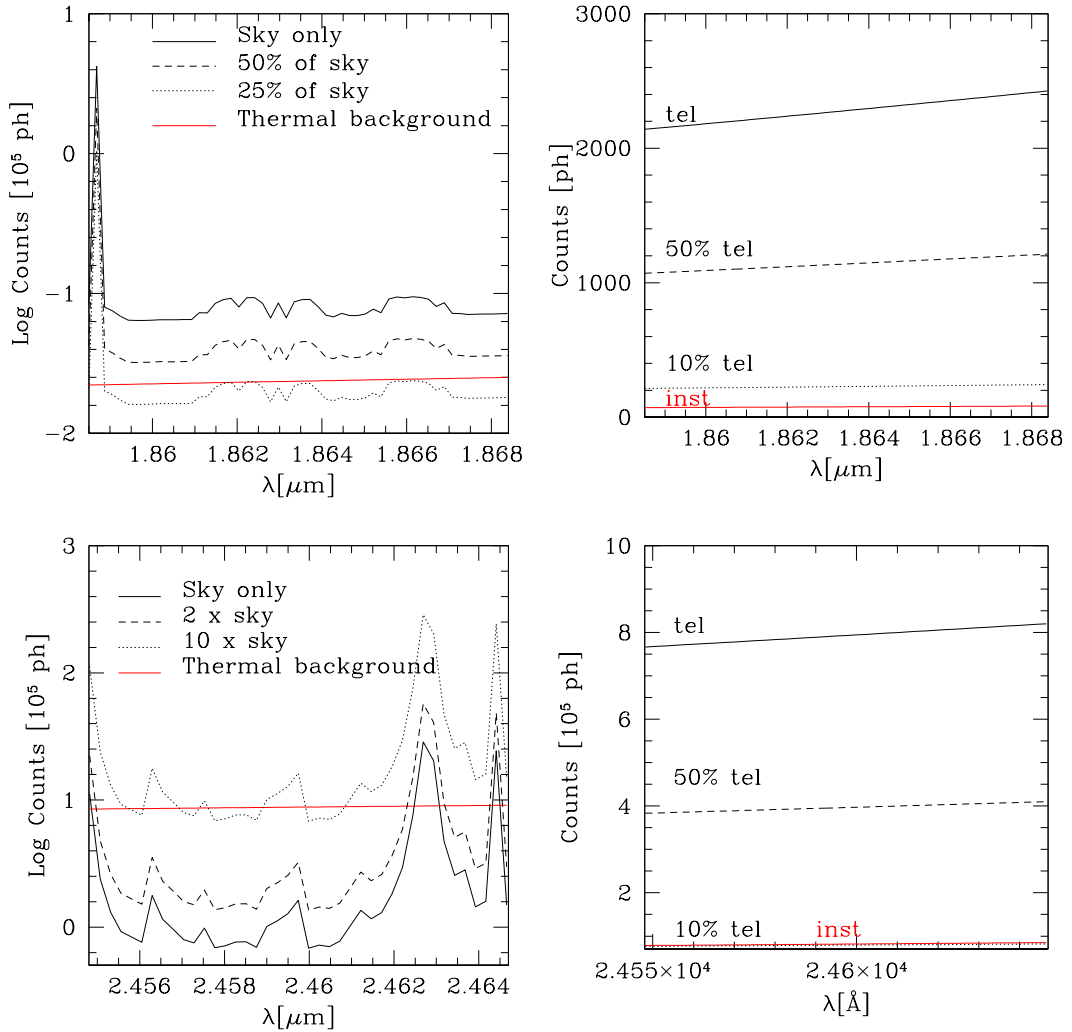
Figure 9: Contributions to the total background in the simulations, at z=4 (upper line) and z=5.6 (bottom line). *Left column:* comparisons between the sky contribution (continuum and OH sky lines, in black) and the total thermal background (telescope and instrument, in red). *Right column:* comparison between the telescope (black) and instrument (red) contributions to the total thermal background.

(2006), with a read-out-noise of 2.3 e/pix and a dark current of 0.01 e/s/pix. Its thermal background, bias, and saturation threshold were neglected. Because observations of distant galaxies in the NIR are generally not limited by the detector noise, we did not explore parameters that have a non-negligible influence only in such a regime, i.e., variations of the individual frame exposure time dit (we chose dit=3600s), and detector characteristics ($dark$ and RON). We assumed a reference case exposure time of $T_{intg} = dit \times ndit$=24 hours, i.e., $ndit$=24.

Global throughput: We assumed a global throughput t_{transm}=20%, detector QE included. The official baseline assumes a transmission of 90-95% for the 5 mirror design telescope and a QE of 90%. The official requirements for EAGLE specifies a

throughput of at least 35%, including the detector QE. Therefore, according to the baseline, the global throughput should be 31%, which is larger that our assumption. This will be further discussed in Sect. 3.5. The integrated number of photons reaching the detector is a degenerated function of some parameters which have no impact on the spatial or spectral resolution, i.e., T_{intg}, t_{transm}, EW_0, and D. Therefore, we chose not to explore variations in global transmission, which can be directly derived by analogy with variations of associated degenerated parameters.

PSF model: The coupling between the AO system and the 3D spectrograph is captured through the AO system PSF. Therefore, it is a crucial element that needs to be carefully simulated, and cannot be approximated by, e.g., a simple Gaussian. Given the multiplex requirements for the present science case, only GLAO and MOAO have been considered. All PSFs include the effect of telescope aperture, but neglect the effects of the central obscuration and spiders. They were generated at the central wavelength of the corresponding filter (e.g., 1.65 microns for the H band), and the difference between this wavelength and the actual wavelength where the emission line is observed (e.g., 1.86 μm for [OII] at z=4) was neglected.

GLAO PSFs were taken from the official DRM *ftp* depository. These PSFs were generated by M. Le Louarn at ESO using an end-to-end code and the official DRM baseline assumptions (v1). Of note, these PSFs correspond to a total integration time of 4 seconds and therefore include non-negligible speckle noise.

MOAO PSFs were simulated using an analytical code (calibrated against an end-to-end code) by B. Neichel (GEPI-Obs. de Paris/ONERA) and T. Fusco (ONERA), which has the advantage of producing PSFs free of speckle noise, i.e., more representative of long-exposure PSFs (Neichel et al., 2008). Briefly, we used assumptions as close as possible to the assumptions used for GLAO PSF modeling: the pitch (inter-actuator distance) was assumed to be 0.5m ($\sim$84$\times$84 actuators in the pupil plane), with a reference seeing of 0.8 arcsec and an outer-scale of the turbulence L_0=25m; the same 10 turbulent layer C_n^2 profile that the one used for GLAO PSFs was considered. The wavefront was measured using three guide stars (assumed to be natural guide stars, i.e., specific issues related to laser guide stars like, e.g., the cone effect, were neglected), located on a equilateral triangle asterism.

In order to sample different performances for the MOAO and GLAO systems, different asterism sizes were considered (see Tab. 4). The PSFs were systematically estimated on-axis. It is beyond the scope of this report to study in detail the coupling of the MOAO with 3D spectroscopy; such a study can be found in Puech et al. (2008b). Of interest here is that in most cases, the coupling between the MOAO system and the IFU pixel scale is such that the spatial resolution is set by the latter because the PSF FWHM is smaller than twice the IFU pixel scale. Improving the MOAO correction further does not provide any gain in spatial resolution but still improves the Ensquared Energy in a spatial element of resolution, hence the SNR. This justifies the usual choice of characterizing the EE in an aperture equal to twice the pixel size.

We chose reference PSFs for both AO systems as close as possible of the middle of the range of EE performances. Hence, the H-band MOAO reference PSF has EE=45.62% (in 100 mas), while the H-band GLAO reference PSF has EE=8.15%

GLAO FoV(')	EE in 100 mas	MOAO FoV(')	EE in 100 mas
1	15.00	0	63.59
2	12.51	0.25	56.13
5	8.15	0.5	45.62
10	6.04	1.0	33.73
15	5.31	2.0	27.24
		3.0	24.09
		4.0	23.06
		5.0	22.67

Table 4: Sets of GLAO and MOAO PSFs generated for the simulations. The asterism size (dubbed "FoV", i.e., the position of guide stars) is varied in order to produce a range of EE sampling typical corrections. All values were measured in the H-band with a seeing of 0.8 arcsec.

(in 100 mas). Unless stated otherwise (see Sect. 3.1.2), these two PSFs are those used in the simulations.

2.4 Outputs

For each simulation, the following FITS files were produced:

- A data-cube at high spatial resolution and high spatial sampling: this is the original data-cube produced from the set of four maps, once it has been rescaled in terms of size and flux (see Sect. 2.2.2);

- A data-cube at high spatial sampling but with degraded spatial resolution: identical to the previous data-cube but with all spectral channels convolved by a PSF. Hence, its spatial resolution is degraded accordingly to the simulated AO system performances;

- An IFU data-cube: this is the final product of the simulation, which corresponds to mock observations;

- An IFU data-cube without noise and PSF effects;

- A total background spectrum (sky continuum, OH sky lines, and total thermal background);

- A thermal background spectrum;

- An SNR data-cube, which gives the expected SNR for each pixel of the IFU data-cube. This spectroscopic SNR is derived as follows:

$$SNR(i_x, j_y, k_\lambda) = \frac{O(i_x, j_y, k_\lambda) * \sqrt{ndit}}{\sqrt{O(i_x, j_y, k_\lambda) + S(i_x, j_y, k_\lambda) + ron^2 + dark}},$$

where $O(i_x, j_y, k_\lambda)$ and $S(i_x, j_y, \lambda)$ are respectively the object and sky flux per dit (after accounting for atmospheric transmission) in the spatial position

(i_x, j_y) of the data-cube (in pixels), and at the spectral position k_λ along the wavelength axis (in pixels). In the following, the "maximal SNR in the emission line in the pixel (i_x, j_y)" refers to $\text{MAX}_{k_\lambda}[SNR(i_x, j_y, k_\lambda)]$, and the "spatial-mean SNR" refers to the average of this quantity over the galaxy diameter.

The main parameters used for a given simulation were recorded in the headers of the corresponding FITS files.

In a second step, for each simulated data-cube, the analysis pipeline produced the following FITS files:

- A data-cube that contains all the fits to the emission lines;

- An emission line flux map;

- A velocity field;

- A velocity dispersion map;

- A map of the kinematical SNR_{kin};

- A map of the maximal SNR, i.e., the SNR at the peak of the emission line within each spaxel of the simulated IFU data-cube. A spatial-mean value is written down into the header (see above).

3 Results of Simulations

3.1 Simulation runs

Unless stated otherwise, parameters are by default set to their reference values as described in Sect. 2.3.

3.1.1 Influence of AO correction

We explore the influence of the AO correction by increasing the EE in a given aperture as described in Sect. 2.3.2 (see Tab. 4), for two types of AO systems, i.e., GLAO and MOAO. Simulations were done for all morpho-kinematical templates in the MOAO case, and for the two UGC5253 and Major merger templates in the GLAO case.

3.1.2 Influence of technical and physical parameters

Simulations were performed for five distinct stellar masses, as described in Tab. 3, and in two different runs, as described in Tab. 5 and 6.

z	Δ_{pix} (mas)	Morpho-kin. Template	EW_0 (Å)	R	D (m)
4	25	UGC5253-Major merger	30	5000	42
	50	UGC5253-Major merger	30	5000	42
	50	UGC5253-Major merger	15	5000	42
	50	UGC5253-Major merger	30	10000	42
	50	UGC5253-Major merger	30	2500	42
	75	UGC5253-Major merger	30	5000	42
	50	UGC5253-Major merger	30	5000	30

Table 5: Technical and physical parameters investigated in the first run of simulations. All other parameters are set to their reference values as described in Sect. 2.3

z	T_{intg} (hr)	Δ_{pix} (mas)	AO correction	Morpho-kin. Template	Seeing (arcsec)
2	8	50	MOAO	ALL	0.8
	24	50	GLAO	ALL	0.8
			MOAO	ALL	0.8-0.95
4	8	50	MOAO	ALL	0.8
	24	50	GLAO	ALL	0.8
			MOAO	ALL	0.8-0.95
5.6	8	50	MOAO	ALL	0.8
	24	50	GLAO	ALL	0.8
			MOAO	ALL	0.8-0.95

Table 6: Technical and physical parameters investigated in the second run of simulations. All other parameters are set to their reference values as described in Sect. 2.3

3.2 Analysis

3.2.1 Influence of AO correction

The spatial-mean SNR obtained for the reference case (H band) as a function of Ensquared Energy in a 100 mas aperture is plotted in Fig. 10. This figure shows that all simulations approximately fall along the same curve, independently of the AO type, although different codes (end-to-end vs. analytical) were used (see Sect. 2.3). This means that all PSFs can be safely compared. For comparison, to the GLAO and MAO PSFs described in Sect. 2.3, we have added MCAO PSFs (with 3DMs and asterisms of 0.5 and 5 arcmin with corrections derived at 0, 0.5,2, and 2.5 arcmin with relative to the center of the FoV) and LTAO PSFs (FoV of 45 arcsec, on axis). The PSFs picked up as representative performances of the GLAO and MOAO modes have been encircled using a red ellipse (see Sect. 2.3). In the H band, they can be considered as well representative of the AO performance within a range of $\sim \pm 2$ in SNR for MOAO, and $\sim \pm 3$ for GLAO. A systematic study of the impact of EE on the kinematics of distant galaxies can be found in Puech et al. (2008b). Of interest here is that the reference MOAO PSF, with an EE of 45.62% in an aperture

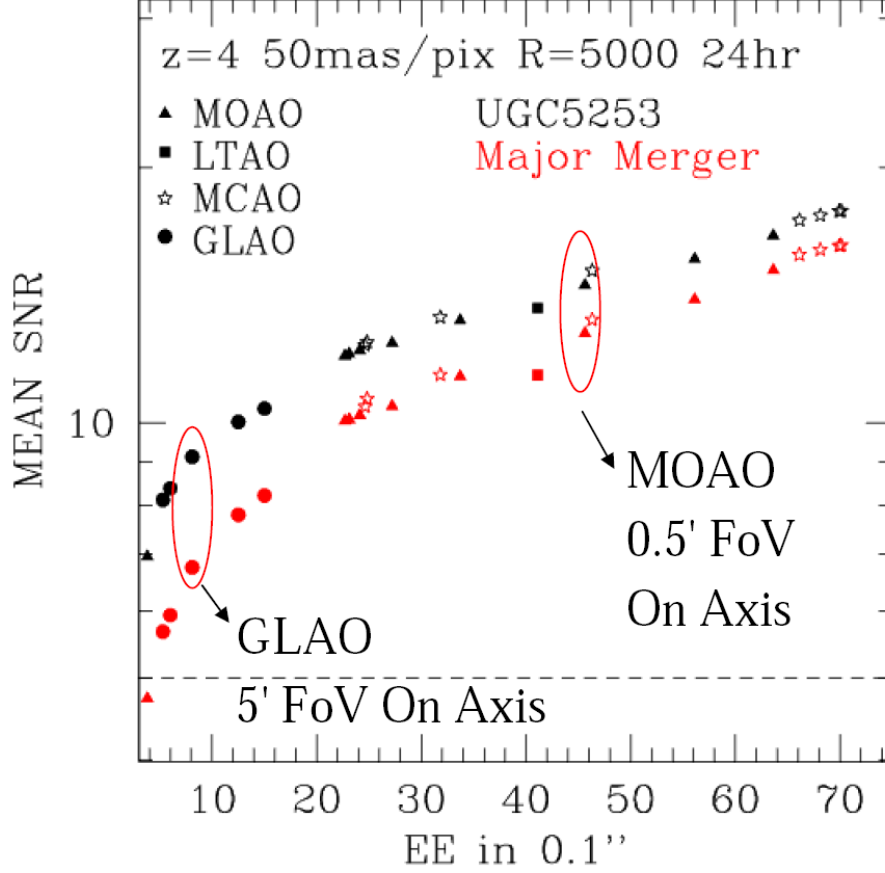of 100 mas is above the minimal requirements derived in this study.

Figure 10: Spatial mean SNR obtained for the reference case (H band) as a function of Ensquared Energy in a 100mas aperture for different type of AO systems. The black points correspond to a rotating disk template, while red points correspond to a major merger template. The left most symbols represent the seeing-limited case.

3.2.2 DRM STEP 1: 3D detection

We adopt a lower limit in SNR of $SNR_{min} = 5$ (spatial-mean SNR in the emission line, see Sect. 2.4) for the 3D detection of distant galaxies. The SNR obtained as a function of the observational parameters and mass is shown in Fig. 11. From this figure, ones finds that the minimal SNR scales as follows:

$$SNR_{min} = 5 \times \left(\frac{T_{intg}}{24h}\right)^{0.5} \left(\frac{D}{42m}\right) \left(\frac{EW_0}{30\mathring{A}}\right) \left(\frac{R}{5000}\right)^{-0.5} \left(\frac{\Delta_{pix}}{50mas}\right)$$

This scaling is the one expected in a background-limited regime. As discussed in Sect. 2.3, T_{intg} and the total instrument transmission (not explicitly explored by simulations) follow the same scaling.

Figure 12 gives the stellar mass that can be reached as a function of redshift for MOAO corrections and a seeing of 0.8 arcsec for $SNR_{min} = 5$ (black line). One can
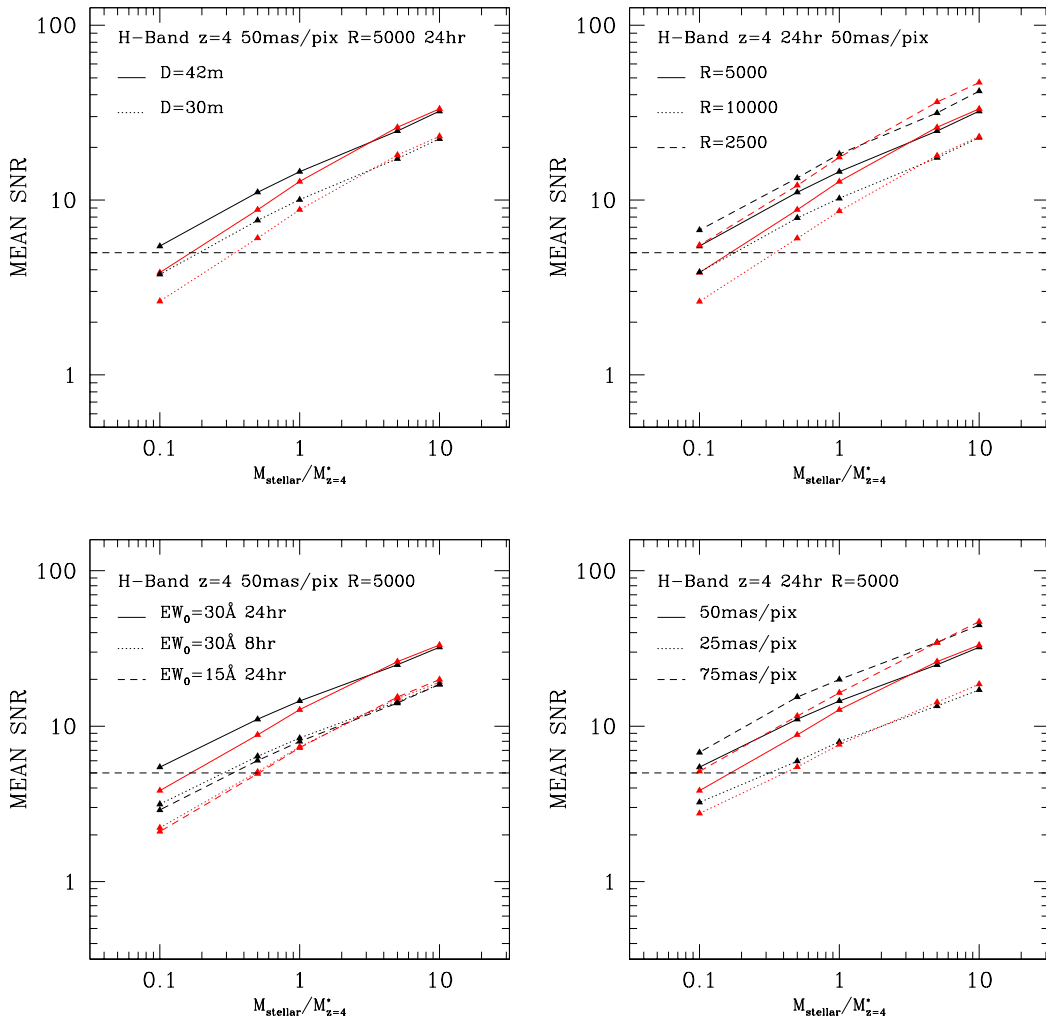
21

Figure 11: Spatial-mean SNR for different stellar masses at z=4 depending on observational parameters. *Upper-left panel:* influence of telescope diameter. *Upper-right panel:* influence of spectral resolution. *Lower-left panel:* influence of integration time and EW_0. *Lower-right panel:* influence of pixel size. In all panels, the stellar-mass ranges from 0.1 to 10 M*, black lines represent simulations of a rotating disk, and red lines represent simulations of a major merger.

see that the limit in stellar mass grows exponentially with redshift:

$$\frac{M_{lim}}{M_*} \simeq 3.3 \times 10^{-6} \exp\left(\frac{z}{0.37}\right) - 0.1,$$

which is due to the exponentially increasing contribution of the thermal background from the telescope in the NIR (see right panel in Fig. 12). Noteworthy, the mass limit evolves quite smoothly with redshift up to z∼4-4.5: this means that this limit does not depend strongly on input parameters like, e.g., seeing (see the blue curve for a 0.95 arcsec), or AO correction (see the red curve for GLAO corrections). It is not surprising that MOAO and GLAO give similar results, as the SNR considered here is a spatial-mean over the galaxy diameter, which does not take into account differences

in terms of spatial resolution (see next Section). One can adopt $SNR_{min} = 10$ (instead of 5) without impacting strongly the resulting mass limit.

It is useful to summarize Fig. 12 by deriving the redshift up to which the Galaxy Stellar Mass Function (GSMF) can be probed down to M_*, as galaxies having such a stellar mass at a given z are those contributing the most to the stellar mass density at this redshift. From Fig. 12, one can see that *the GSMF can be probed down to M_* up to z=4, independently of the SNR limit, AO correction, and seeing conditions.*
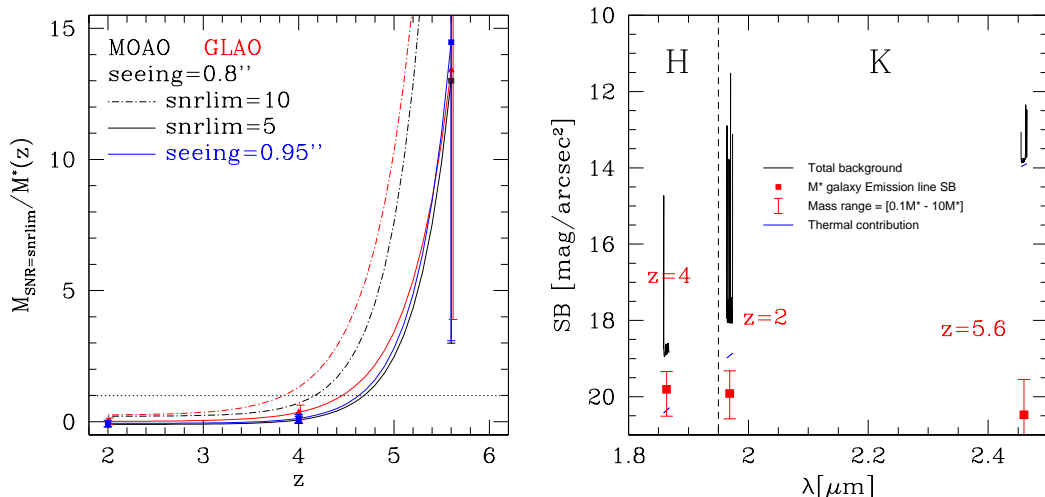

Figure 12: *Left:* Stellar mass limit that can be reach at a given SNR_{min} as a function of redshift, AO correction, and seeing. Error-bars represent the range of mass limit obtained when considering all the morpho-kinematical templates. *Right:* Comparison between the median emission line surface brightness of the simulated galaxies (in red) with that from the thermal background (telescope and instrument, blue lines) and total background (thermal plus continuum and OH sky lines, black lines).

3.2.3 DRM STEP 2: Large scale motions

Because we are interested in recovering large-scale motions, it is sufficient to characterize the SNR over the galaxy size, using a simple spatial mean as defined in Sect. 2.4. Using MOAO, it has been suggested that a spatial-mean SNR of 5 is a minimum to recover large-scale motions and distinguish between a major merger and a rotating disk (Puech et al., 2008b). In Table 7, we give the SNR obtained for a range of stellar-mass using the reference case and MOAO or GLAO corrections. According to this table, it should be feasible to distinguish between both kinds of templates down to $0.5M_*$ at z=4 using MOAO. A direct visual inspection of the simulations confirms this threshold (see Fig. 13).

Using GLAO, Table 7 suggests that the same distinction could be made down to M_* at z=4 (instead of $0.5M_*$ using MOAO). Because GLAO corrections smooth out much more kinematic details than MOAO, it is therefore difficult to distinguish a major merger from a rotating disk down to the same limit in stellar masses/SNR:

$M_{stellar}$ (in $M_*(z)$)	SNR w/ MOAO z=4	SNR w/ GLAO z=4	SNR w/ MOAO z=5.6	SNR w/ GLAO z=5.6
0.1	5.45-3.85	2.58-2.53	0.78-0.44	0.37-0.18
0.5	11.09-8.80	6.41-4.40	1.49-1.23	0.90-0.60
1.0	15.54-12.76	9.12-6.75	2.07-1.60	1.28-0.86
5.0	24.84-26.07	17.89-16.46	3.92-3.75	2.76-2.20
10.0	32.24-33.27	24.21-23.46	5.14-5.13	3.66-3.15

Table 7: Spatial-mean SNR obtained for simulations of the reference case as a function of mass and redshift, for MOAO and GLAO corrections. The first value corresponds to simulations with a rotating disk template (UGC5253), while the second value corresponds to simulations with a major merger template.

it is indeed difficult to visually distinguish non-circular motions in the $0.5M_*$ major merger simulations at z=4 with GLAO, as shown in Fig. 13.

At z=5.6, the much higher background makes any distinction very difficult, and at best limited to the highest mass galaxies, as suggested by Tab. 7 and Fig. 14.

In summary, *provided a SNR of 5, it is possible, using MOAO, to recover large scale motions of galaxies and distinguish between different dynamical states at least up to z=4 and down to $M_{stellar}=0.5M_*$. GLAO provides very similar performances, although at lower spatial resolution, which limits the recovery of the dynamical state down to $\sim M_*$ at z=4. At higher redshift, the lost of SNR induced by the increasing contribution of the thermal background of the telescope, limits the recovery of large-scale motions to very massive systems.*

3.2.4 DRM STEP 3: Rotation Curves

In Figure 15, we show rotation curves extracted from simulations at z=2 and z=4 using the UGC5253 rotating disk template. To focus on spatial features, we did not try to fit the inclination, and held this parameter fixed during the fitting to the velocity field. We adopted a simple arctan rotation curve, which is fully described by two parameters (Courteau, 1997).

At z=2, only MOAO can more or less recover the rising part of the RC. Due to its much lower spatial resolution ($FWHM_{GLAO}$=161mas and $FWHM_{MOAO}$=11mas), GLAO induces a beam smearing-like effect, as in HI observations of local galaxies. However, the spatial sampling of the IFU (50mas/pix) limits the spatial resolution of the observations (to $\sim$0.1 mas) and does not allow to recover the true shape of the RC. Compared to the best RC that one can recover at this spatial scale (see the black dashed line), MOAO and even GLAO does not induce any further bias in terms of rotation velocity. However, to recover the true rotation velocity, one will need to use numerical simulations, as it is already the case in lower redshift kinematic studies of distant galaxies (see, e.g., Flores et al. 2006; Förster-Schreiber et al. 2006; Puech et al. 2008).

At z=4, the lack of spatial resolution will limit the study of rotation curves to super-M_* rotating disks, as seen in Fig. 15. At these redshifts, only MOAO will provide enough spatial resolution to limit biases in recovering the rotation velocity
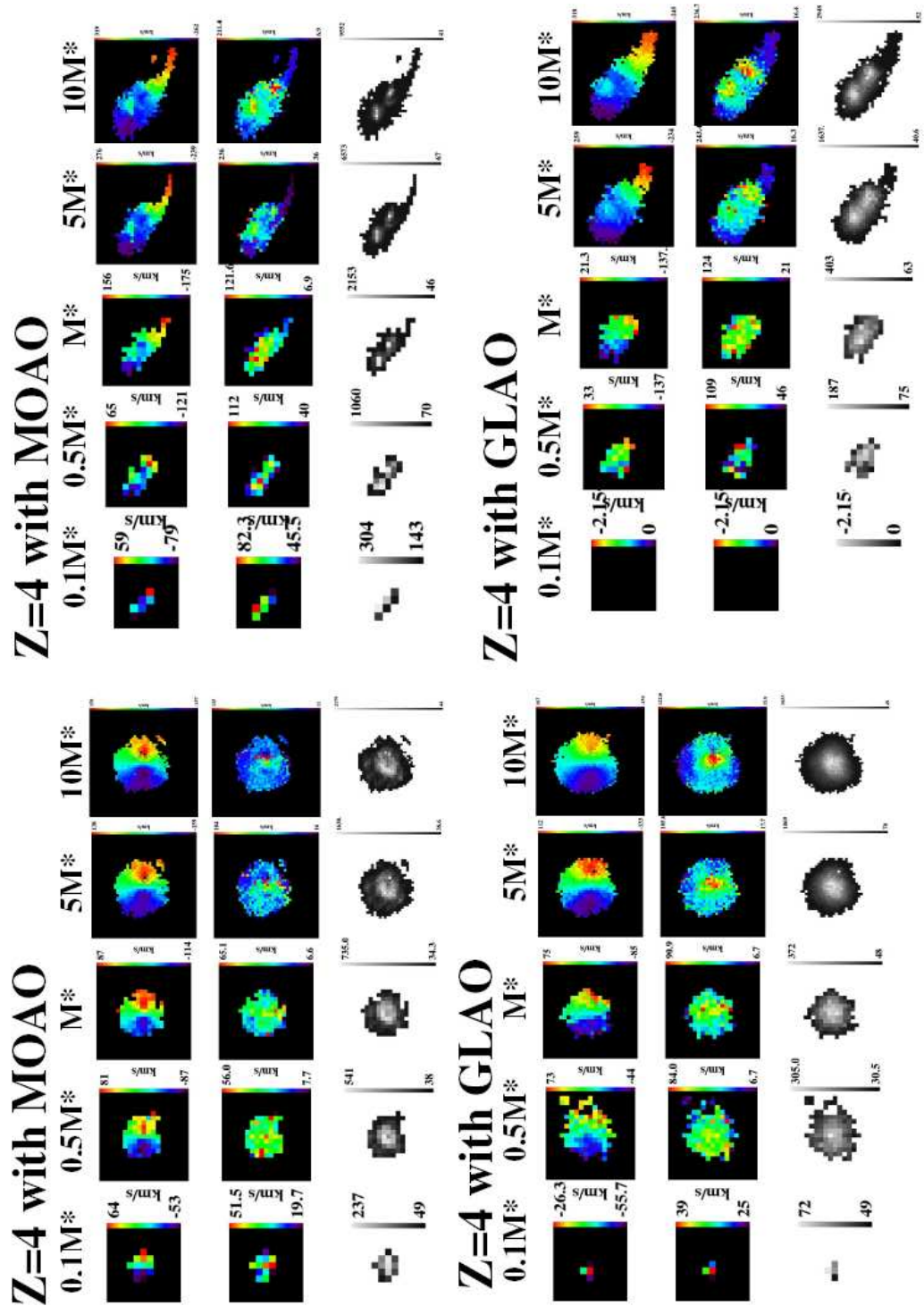
Figure 13: Results of simulations at z=4 with MOAO (upper panels) and GLAO (bottom panels). Each panel shows velocity fields (first line), velocity dispersion maps (second lines), and emission line maps (third lines) for different stellar masses (from $0.1M_*$, first column, to $10M_*$, last column). The two panels on the left show simulations using a rotating disk template (UGC5253), while the two panels of the right show simulations for a major merger.
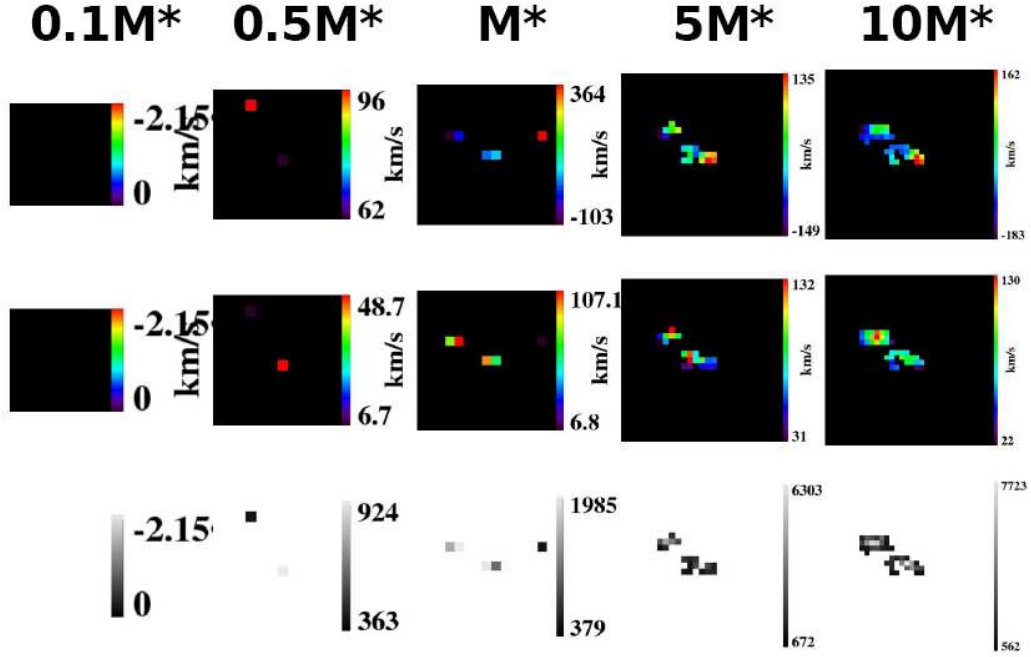
Figure 14: Results of major merger simulations at z=5.6 using MOAO. *From top to bottom:* velocity fields (first line), velocity dispersion maps (second lines), and emission line maps (third lines) for different stellar masses (from 0.1M$_*$, first column, to 10M$_*$, last column).

or the rising part of the RC.

In summary, *the recovery of the whole shape of the RC will be limited to z∼2, using MOAO. The recovery of the true rotation velocity will require numerical simulations, which is already the case in lower-z studies. At higher redshifts, such measurements will be limited to super-M$_*$ galaxies.*

3.2.5   DRM STEP 4: Detailed kinematics

We present results of Jeans-unstable clumpy disks in Fig. 16. Clumps can clearly be distinguished in galaxies more massive than M$_*$ at z=4, using MOAO (see emission line maps). Using GLAO does not allow to identify these clumps anymore: all clumps are smoothed together in the emission line map. One can still recover non-circular motions in the velocity fields, but without clear morphological signature, it is difficult to identify the underlying cause of this perturbation. At higher redshift, the limited SNR does not allow to recover such clumps anymore, even in very massive galaxies.

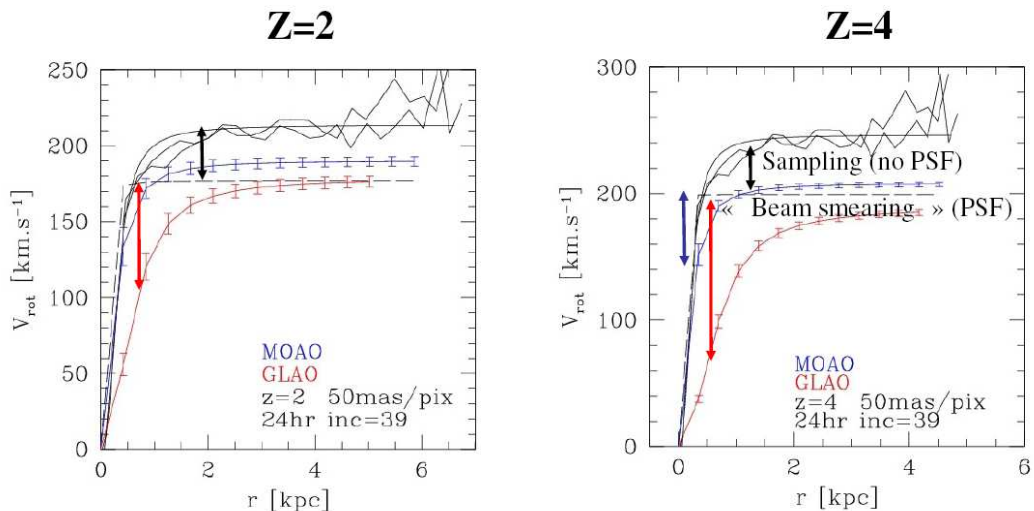In summary, *it is possible to recover clumps in rotating disks down to z=4, M$_*$ galaxies using MOAO.*

Z=2   **Z=4**

Figure 15: Rotation curve of a z=2, M_* galaxy (left panel), and a z=4, $5M_*$ galaxy (right panel). The black lines represent the original z=0 rotation curve rescaled to the size of simulated z=2 and z=4 galaxies; the rotation curve on each side of the galaxy is shown, along with an arctan fit. The rotation curve obtained using MOAO is shown in blue, while the one obtained using GLAO is shown in red. Error-bars represent only the uncertainty associated to the two parameters of the arctan function, and do not take into account uncertainties associated to other kinematic parameters like the dynamical center or the Principle Axis. The black dashed line represent the rotation curve obtained in simulations without PSF: they correspond to the best rotation curve that one can obtain at the pixel scale of the simulations (50mas/pix).

3.3   Compliance with figures of merit

The goal of the survey was to study N_{gal} ~1000 galaxies at $2 \leq z \leq 6$ with $0.1 \leq M_{stellar} \leq 5 \times 10^{11} M_\odot$ in less than 100 nights. We adopt the following assumptions as a typical observational strategy for this science case:

- reference case with R=5000 and Δ_{pix}=50mas (see Sect. 2.3);

- MOAO corrections;

- Mauna-Kea-like background, as described in Sect. 2.3;

- a limiting SNR of 10 (10-σ detection);

- overheads of 30% (i.e., overhead factor OH=1.3);

- three redshift bins (z=2, z=4, and z=5.6) and three mass bins per redshift bin (~$0.5M_*$,~ M_*, and ~$5M_*$), except for the $z = 5.6$ bin, which has only two mass bins (~ M_*, and ~$5M_*$), since we are interested in galaxies having $0.1 \leq M_{stellar} \leq 5 \times 10^{11} M_\odot$ and that M_*(z=5.6)=0.8×10^{10}M$_\odot$. The structure of the survey is illustrated in Fig. 17;
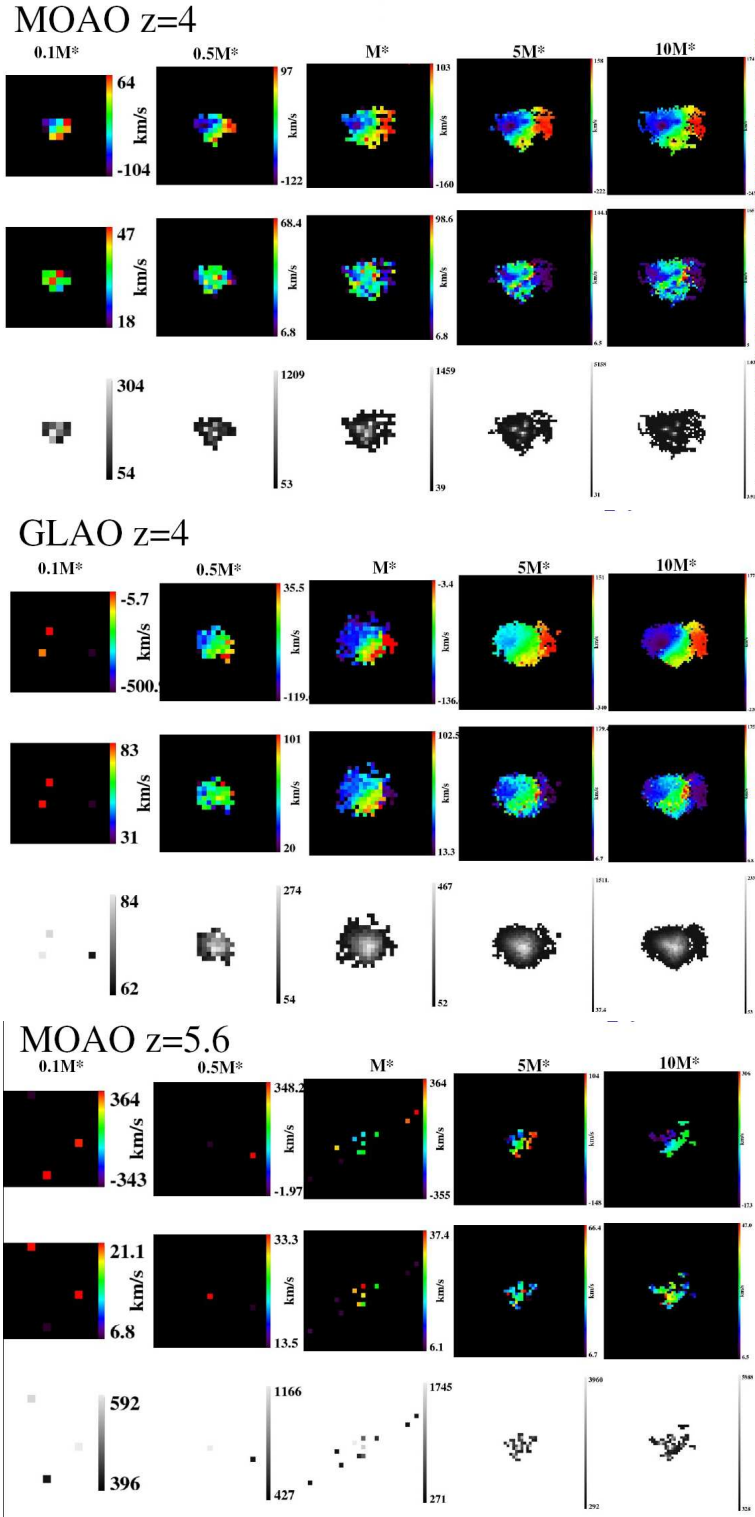
Figure 16: Simulations of clumpy disks at z=4 using MOAO (upper panel), GLAO (middle panel), and MOAO at z=5.6 (bottom panel). In each panel, the first line shows the velocity fields, the second line the velocity dispersion maps, and the third line the emission line maps, for a range of stellar mass (from $0.1M_*$, first column, to $10M_*$, last column).

- the number of galaxies per elementary bin is assumed to be N_{gal}=100, in order to allows one to derive statistics over the morpho-kinematic types within each bin. This translates into total number of galaxies in the survey of $N_{gal} \times N_{bins}$=800.

- Within each bin of the survey, the N_{gal}=100 galaxies can be observed in N_{setups} setups, with N_{setups}=N_{gal}/M where M is the multiplex capability of the instrument. We assume $M \geq 10$, which means that all galaxies in a given bin can be observed in one instrument setup ($N_{setup} = 1$);

- the number of effective observed hours per night is assumed to be 8 hr.

3D survey
of
emission line
galaxies

z=2 - 10 Gyr ago   z=4 - 12 Gyr ago   z=5.6 - 12.6 Gyr ago

~0.5Mstellar/M* ~Mstellar/M* ~5Mstellar/M*   ~0.5Mstellar/M* ~Mstellar/M* ~5Mstellar/M*   ~Mstellar/M*   ~5Mstellar/M*
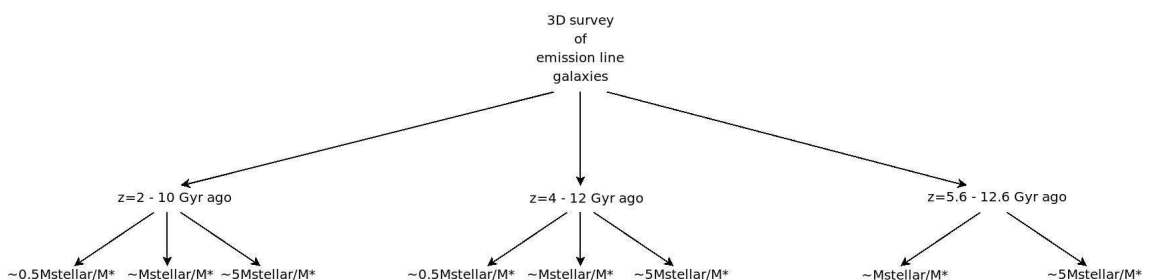
Figure 17: Structure of the survey.

The corresponding integration time, in nights, needed in each elementary bin is given in Tab. 8. The great collecting power of the E-ELT is clearly reflected in the time needed to survey ~667 galaxies in the redshift range 2-4, which requires only ~7 nights. Regarding the z=5.6 bin, the large thermal background of the telescope (see Figs. 9 and 12) translates into very large integration times.

T_{intg}	$0.5M_*$	M_*	$5M_*$	Total
z=2	1.2	0.8	0.3	2.3
z=4	2.3	1.4	0.6	4.3
z=5.6	—	66.9	16.39	83.2
Total	3.5	69.1	17.2	89.8

Table 8: Integration time needed to complete the survey, in nights, assuming a multiplex M=125.

The total time survey, in nights, can be expressed as follows:

$$T_{survey}(n) \simeq 90 \Big(\frac{100}{M}\Big) \Big(\frac{SNR_{lim}}{10}\Big)^2 \Big(\frac{N_{gal}}{800}\Big) \Big(\frac{OH}{1.3}\Big)$$

In summary, *with a total integration time of 90 nights, and within the assumptions listed above, it will be possible to:*

- *Observe 800 galaxies with SNR=10 in three redshift bins (2-4-5.6) and three mass bins ($0.5M_*$-$1.0M_*$-$5M_*$), except for the $z = 5.6$ bin, which has two mass bins ($\sim M_*$, and $\sim 5M_*$); all bins have 100 galaxies, which will allow one to do statistics over morpho-kinematic types;*

- *Recover the large-scale motions of galaxies at least up to z=4 and down to $M_{stellar} = 0.5M_*$, i.e., of most galaxies in the survey;*

- *Recover the detailed kinematics of the most massive galaxies (the detection of clumps in rotating disks will be possible down to z=4 M_* galaxies).*

3.4 Sensitivity to input parameters

3.4.1 Impact of telescope

Diameter: MOAO provides only partial seeing corrections, therefore the resulting PSF is dominated by residual atmospheric perturbations. This implies that the telescope diameter does not directly influence the spatial resolution of observations, but only the achieved SNR. The scaling relation of Sect. 3.2.2 shows that there is no breaking point in telescope diameter: with a smaller 30m telescope, one would need two times longer exposures to reach the same SNR.

Thermal background: The telescope is by far the dominant source of background in the K-band. Because the SNR is in a background-limited regime at z=5.6 (see Fig. 12), the telescope thus limits the detectability of sources at very high redshift. Note that in the simulations, we have assumed the most optimistic assumption for the emissivity of the 5-mirror E-ELT design, with $\epsilon_{tel} =5\%$.

3.4.2 Impact of site

Sky background: The sky is the dominant source of background only for $z \leq 4$ observations. Note that in the simulations, we have used a sky model from Mauna Kea, which is ~2 times fainter in the H band that the official DRM Paranal model (see Sect. 2.3.2). As $SNR \propto 1/\sqrt{background}$ in such a regime, a site having two (four) times higher background than the one used in the simulations will reduce the achieved SNR from, e.g., 10 to 7 (5). The impact on high-redshift observations is therefore relatively limited (see Fig. 12).

Seeing: The SNR loss between observations with a seeing of 0.8 arcsec and observations with a seeing of 0.95 arcsec is 5-15%. The strongest impact of worst seeing conditions will be to limit the capability to recover Rotation Curves and detailed kinematics of distant galaxies.

3.4.3 Impact of Instrument

GLAO vs. MOAO: GLAO limits the achievable SNR to lower values, compared with MOAO. As a consequence, the recovery of the large scale motions in distant galaxies using GLAO is limited to higher masses. Any further objective of the DRM will be strongly limited in using GLAO instead of MOAO (e.g., rotation curves, detailed kinematics).

Pixel scale: The choice of the IFU pixel scale drives the spatial resolution of MOAO-fed 3D spectroscopy observations, as in the range of EE provided by MOAO, the PSFs have a FWHM largely smaller than twice the pixel size. Therefore, the choice of the optimal IFU pixel scale is related to the optimal "scale-coupling" between the IFU pixel scale and the spatial scale of the physical feature that one wants to recover using this IFU (Puech et al., 2008b). It can be quantified by using the ratio between the size of this feature (here, the galaxy diameter, as one wants to recover the large-scale rotation) and the size of the IFU resolution element. 3D observations of z∼0.6 galaxies with FLAMES/GIRAFFE have demonstrated that a scale-coupling of about 3 is already enough to recover large-scale motions (Flores et al., 2006). It corresponds to the minimum value necessary to ensure that each side of the galaxy is at least spatially sampled by the IFU at the Nyquist rate. In the z=4 simulations, this minimal scale-coupling leads to a pixel scale of 55mas, 125 mas, and 280 mas for 0.1, 1, and 10 M* galaxies, respectively. Hence, a minimal pixel scale of 50 mas is required if one wants to be able to recover, at least in principle, large-scales motions in z=4 galaxies, and for a large range of stellar-mass.

In Fig. 13, we show the velocity fields, velocity dispersion maps, and emission line maps extracted from the simulations using a 50 mas pixel scale. One can see that the lowest mass case barely provides enough spatial information to clearly distinguish between the rotating disk and the major merger. Even if the scale-coupling is in principle large enough to properly recover large-scale motions, the pixel scale limits the achieved SNR to relatively low values (see Fig. 11). If one only wants to recover large-scale motions in the most massive objects, then an IFU pixel scale of 75 mas can be used, providing more SNR at constant integration time (see Fig. 11).

Spectral Resolution: Appropriate targets in the NIR are usually selected such as they have emission lines that fall in regions free of strong OH lines. This requires a minimal spectral resolution of R∼3000 to resolve OH sky lines with enough accuracy. On the other hand, the highest the spectral resolution, the better the accuracy on the recovered kinematics (see Tab. 9): at least R=5000 is required if one wants to recover the velocity dispersion with no more that 50% of relative uncertainty. This value appears to be a good compromise between the desire to minimize the impact of the OH sky lines and not wanting to over-resolve the line by a large factor: Fig. 11 clearly demonstrates the interest of having the smallest spectral resolution possible, which optimizes the achieved SNR. We estimated that about one third of the H-band is free from strong sky background variations (i.e., larger that 10% of the sky continuum) in continuous windows of at least 200 km/s[1].

Multiplex capability: In Sect. 3.3, we have assumed an optimal multiplex capability M=125. However, it is likely that the future multi-object integral field spectrograph on the E-ELT, EAGLE, will not provide us with a so large multiplex capability. At constant T_{survey}, the relation between the multiplex capability M and the total number of galaxies in the survey is $N_{gal} = 8M$. Therefore, if one assumes

---

[1]This obviously depends on the spectral resolution and sampling of the sky background. These figures were determined using the Mauna Kea sky model, which has a spectral resolution of 0.4 $\overset{\circ}{A}$ and is sampled at the Nyquist rate. This gives a spectral power of resolution R∼22500 at λ=9000$\overset{\circ}{A}$.

SNR	3-4	4-5	5-7	7-10	$\geq$10
R=2500	70km/s-73%	46km/s-59%	31km/s-42%	25km/s-21%	9km/s-9%
R=5000	59km/s-50%	38km/s-42%	31km/s-29%	21km/s-20%	8km/s-8%
R=10000	54km/s-50%	37km/s-36%	57km/s-26%	20km/s-18%	8km/s-7%

Table 9: Accuracy on the velocity (in km/s) and relative accuracy (in %) on the velocity dispersion measurement as a function of spectral resolution (Monte-Carlo simulations).

M=25, only 200 galaxies can be observed in T_{survey}=90n, each bin having 25 galaxies. Such a preliminary survey would certainly provide a very interesting and useful first glimpse of the galaxy mass assembly process as a function of time.

3.5   Limitations

Main limitations are:

- **Variations with wavelength:** most of inputs are currently considered as invariant with wavelength (e.g., throughput, emissivity), because the design of the telescope and the instrument are not fully known at the moment. Simulations shall be updated once these characteristic curves will be known;

- **Range of morpho-kinematical templates:** the real morpho-kinematical range that one would need to sample to be exhaustive is much larger than the one used for the simulations. However, the exact physical conditions in high-redshift galaxies in far from being well known at the moment. Therefore, the authors have intentionally limited simulations to a few motivated cases;

- **Accuracy on the scientific inputs:** most of quantities are not known to a factor better than two. However, simulations are internally-consistent in a sense that neglected corrections on physical quantities are not larger that this factor. For instance, the empirical relations between stellar mass and K-band magnitude are uncertain within a factor two (likely more at z$\geq$4), but the flux correction between the rest-frame wavelength corresponding to the K-band and that of the emission line considered is also less than a factor two (see Sect. 2.3); also, the Tully-Fisher relation appears to evolve smoothly with redshift (a factor two in mass between z=0 and z$\sim$0.6, see Puech et al. 2008);

- **Representative of the simulations:** for simplicity, we have adopted several assumptions that might impact the results of the simulations in terms of SNR (see Sect. 2.3). First, EAGLE specifications suggest that the global through-put might be $\sim$55% higher than assumed, which would translate into a increase of the SNR by $\sim$25%, since $SNR \propto \sqrt{t_{trans}}$. Second, we have neglected the central obscuration of the E-ELT, which leads to overestimate the SNR by $\sim$8%, since $SNR \propto D$. Finally, we have assumed that the [OII] doublet in a single emission line instead of a doublet. The average [OII] line ratio is 1.4 (Flores et al., 2006), which leads to an overestimation of the maximal SNR in the emission line by a 41% at constant flux (based on the crude assumption of

two resolved Gaussians), and in turns leads to overestimate the spatial-mean SNR by the same factor. Therefore, one can estimate that all our assumptions leads to overestimate the spatial-mean SNR by $\sim$24%. We have assumed EW_0=30Å, and since $SNR \propto EW_0$, this means that our simulations would actually correspond to $EW_0 \sim$37Å. Therefore, one should consider that the reference EW_0 is 37Å instead of 30Å, which was chosen as an extrapolation of the *mean* EW_0([OII]) observed at z$\sim$1 (Hammer et al., 1997). This new value is actually closer to the *median* EW_0([OII]) observed at z$\sim$1 (Hammer et al., 1997): such a value is as relevant as the first one, and therefore the adopted simplifications do not impact strongly the results.

4   Concluding Remarks

We have conducted simulations of the "Physics and mass assembly of galaxies out of z$\sim$6" science case exploring a wide range of observational and physical parameters. We have defined figures of merit for this science case despite the inherent complexity of the science goals, derived empirical scaling relations between the signal-to-noise ratio and the main telescope and instrument parameters, as well as a relation between the limit in stellar mass that can be reached for a given signal-to-noise ratio as a function of redshift. We specifically investigated the impact of AO performance on the science goal. We did not identify any breaking points with respect to all parameters (e.g., the telescope diameter), with the exception of the telescope thermal background, which strongly limits the performance in the highest (z>5) redshift bin. We find that the full range of science goals can be achieved with a $\sim$100 nights program on the E-ELT. We stress that several assumptions and guided guesses had to be made on both the observational conditions and physical characteristics of distant galaxies under study. This introduces an inherent uncertainty, which can be mitigated with future simulations as the telescope design will be consolidated and more details about the physics of high-z galaxies will become available.

References

Amram, P., Adami, C., Balkowski, C., et al. 2002, Ap&SS, 281, 393

Barden, M., Rix, H.-W., Somerville, R.S., et al. 20005, ApJ, 635, 959

Beauvais, C., & Bothun, G. 1999, ApJS, 125, 99

Blais-OUellette, S., Amram, P., & Carignan, C. 2001, AJ, 121, 1952

Bournaud, F., Elmegreen, B.G., Elmegreen, D.M. 2007, ApJ, 670, 237

Bournaud, F., Daddi, E., Elmegreen, B.G. 2008, ApJ, 486, 741

Bouwens, R.J., Illingworth, G.D., Blakeslee, J.P., et al. 2004, ApJ, 611, 1

Courteau, S. 1997, AJ, 114, 2402

Courteau, S., Dutton, A.A., van den Bosch, F.C., et al. 2007, ApJ, 671, 203

Cox, T.J., Jonsson, P., Primack, J., et al. 2006, MNRAS, 373, 1013

Dahlen, T., Mobasher, B., Dickinson, M., et al. 2007, ApJ, 654, 172

Epinat, B., Amram, P. Marcelin, M., et al. 2008, MNRAS, in press, astro-ph/0805.0976

Ferguson, H.C., Dickinson, M., Giavalisco, M. et al. 2004, ApJ, 600, 107

Finger, G., Garnett, J., Bezawada, N., et al. 2006, Nuclear Instruments & Methods in Physics Research A, 565, 241

Flores, H., Hammer, F., Puech, M., et al. 2006, A&A, 455, 107

Förster-Schreiber, N., Genzel, R., Lehnert, M.D., et al. 2006, ApJ, 645, 1062

Fried, D.L. 1981, JOSA, 72, 52

Fuentes-Carrera, I., Rosado, M. Amram, P., et al. 2004, A&A, 415, 451

Garrido, O., Marcelin, M., Amram, P. et al. 2002, A&A, 387, 821

Garrido, O., Marcelin, M., Amram, P. 2004, A&A, 349, 225

Genzel, R., Tacconi, L.J., Eisenhauer, F., et al. 2006, Nature, 442, 786

Grazian, A., Fontana, A., de Santis, C., et al. 2006, A&A, 449, 951

Hammer, F., Flores, H., Lilly, S.J., et al. 1997, ApJ, 481, 49

Hammer, F., Puech, M., Chemin, L., et al. 2007, ApJ, 662, 322

Kinney, A.L., Calzetti, D., Bohlin, R.C., et al. 1996, ApJ, 467, 38

Laporte, P., Chemla, F., Puech, M. et al. 2008, SPIE Proc. Vol. 7014, in press

Neichel, B., Fusco, T., Conan, J.-M., et al. 2008, Proc. SPIE Vol. 7015, in press

Puech, M., Hammer, F., Flores, H., et al. 2006, A&A, 455, 119

Puech, M., Flores, H., Hammer, F., et al. 2006, A&A, 455, 131

Puech, M., Flores, H., Hammer, F., et al. 2008, A&A, 484, 173

Puech M., Flores, H., Lehnert, M., et al., MNRAS, accepted

Roddier, F. 1981, Progress in Optics, 19, 281

Sarzi, M., Falcon-Barroso, J., Davies, R.L., et al. 2006, MNRAS, 366, 1151

Appendix

The DRM proposal C10-1 "The Physics and Mass Assembly of Galaxies out to z∼6" is attached herewith.